646 *Inorg. Chem.* **2010**, *49*, 646–658
DOI: 10.1021/ic901846u

Inorganic Chemistry
Article

Spin Interaction in Octahedral Zinc Complexes of Mono- and Diradical Schiff and Mannich Bases

M. Orio,[†] C. Philouze,[‡] O. Jarjayes,*[,‡] F. Neese[†] and F. Thomas*[,‡]

[†]*Institute for Physical and Theoretical Chemistry, Universität Bonn, Wegelerstrasse 12, D-53113 Bonn, Germany and* [‡]*Département de Chimie Moléculaire, Chimie Inorganique Redox Biomimétique (CIRE), UMR-5250, Université JosephFourier, BP 53, 38041 Grenoble Cedex 9, France*

Received September 18, 2009

The four Schiff bases 2-*tert*-butyl-4-methoxy-6-[(pyridin-2-ylmethylimino)methyl]phenol, 2,4-di-*tert*-butyl-6-[(pyridin-2-ylmethylimino)methyl]phenol, 2-*tert*-butyl-4-methoxy-6-(quinolin-8-yliminomethyl)phenol, and 2,4-di-*tert*-butyl-6-(quinolin-8-yliminomethyl)phenol) as well as one Mannich base, *N*,*N*′,*N*,*N*′-bis[(2-hydroxy-3,5-di-*tert*-butylbenzyl)(2-pyridylmethyl)]ethylenediamine, and their zinc bis-phenolate complexes **1**−**5**, respectively, have been prepared. The complexes **4** and **5** have been characterized by X-ray diffraction crystallography, showing a zinc ion within an octahedral environment, with a cis orientation of the phenolate moieties. **1**−**5** exhibit in their cyclic voltammetry curves two anodic reversible waves attributable to the successive oxidation of the phenolates into phenoxyl radicals. Bulk electrolysis at ca. +0.1 V affords the zinc-coordinated monophenoxyl radical species $(\mathbf{1}^{\bullet})^{+}$−$(\mathbf{5}^{\bullet})^{+}$ characterized by UV−vis absorption bands at 400−440 nm. The more stable radicals are $(\mathbf{3}^{\bullet})^{+}$ and $(\mathbf{4}^{\bullet})^{+}$ (half-life higher than 90 min at 298 K), likely due to the increased charge delocalization within the quinoline moieties. These species exhibit a significant additional near-IR band ($\varepsilon > 1650\ M^{-1}\ cm^{-1}$) attributed to a CT transition. In the two-electron-oxidized species $(\mathbf{1}^{\bullet\bullet})^{2+}$−$(\mathbf{5}^{\bullet\bullet})^{2+}$ the radical spins present a weak magnetic coupling. EPR reveals an antiferromagnetic exchange interaction for $(\mathbf{1}^{\bullet\bullet})^{2+}$−$(\mathbf{4}^{\bullet\bullet})^{2+}$, whereas an unusual ferromagnetic exchange coupling is operative in $(\mathbf{5}^{\bullet\bullet})^{2+}$. The weak magnitude of experimental $|J|$ values (within the 1−5 cm^{-1} range) as well as their sign could be well reproduced by DFT calculations at the B3LYP level. The small energy gap between the ground and the first excited spin states allows us to investigate the zero-field splitting (ZFS) of the triplet by EPR spectroscopy. This parameter is found to be axial for all systems, with $|D|$ values of 0.0163 cm^{-1} for $(\mathbf{1}^{\bullet\bullet})^{2+}$, 0.0182 cm^{-1} for $(\mathbf{2}^{\bullet\bullet})^{2+}$, 0.0144 cm^{-1} for $(\mathbf{3}^{\bullet\bullet})^{2+}$, 0.0160 cm^{-1} for $(\mathbf{4}^{\bullet\bullet})^{2+}$, and 0.0115 cm^{-1} for $(\mathbf{5}^{\bullet\bullet})^{2+}$. The trend between experimental ZFS is confirmed by DFT calculations, which give further insight regarding its sign (negative for all the compounds). Lower ZFS values are obtained for $(\mathbf{2}^{\bullet\bullet})^{2+}$ compared to $(\mathbf{1}^{\bullet\bullet})^{2+}$ (and also for $(\mathbf{4}^{\bullet\bullet})^{2+}$ compared to $(\mathbf{3}^{\bullet\bullet})^{2+}$), which can be interpreted by an increased delocalization of the spin density over the methoxy para substituent. Significant spin population on the quinoline also contributes to a lowering of the $|D|$ value, as observed when $(\mathbf{3}^{\bullet\bullet})^{2+}$ is compared to $(\mathbf{1}^{\bullet\bullet})^{2+}$ (and also when $(\mathbf{4}^{\bullet\bullet})^{2+}$ is compared to $(\mathbf{2}^{\bullet\bullet})^{2+}$).

Introduction

Free radicals are used by number of metalloproteins as an additional redox center to facilitate electron transfer and improve their reactivity.[1] Galactose oxidase (GO) belongs to this class of radical metalloprotein. Its particularity resides in the fact that the radical (the tyrosyl radical Tyr272$^{\bullet}$) is directly coordinated, and antiferromagnetically exchange coupled, to the metal ion (copper(II)).[2] It catalyzes the oxidation of primary alcohols into aldehydes, with concomitant reduction of dioxygen into hydrogen peroxide. The cooperativity between the metal ion and the radical to perform the oxidation reaction is evident from the proposed catalytic mechanism: in a first step the copper(II) ion binds the substrate by its hydroxyl group. The Lewis acidity of the metal and the presence of a neighboring base facilitate its deprotonation. The energy of the C_{α}−H bond to be broken is subsenquently lowered, making hydrogen abstraction by the tyrosyl radical easier.

In order to better understand the fundamentals of this metal-radical chemistry, we and other groups have developed several complexes involving copper-coordinated redox-active

*To whom correspondence should be addressed. F.T.: fax, (+33) 476 514 846; e-mail, Fabrice.Thomas@ujf-grenoble.fr.

(1) *Chem. Rev.* **2003**, *103* (6) (special issue devoted to radical metalloenzymes).

(2) For reviews, see: Whittaker, J. W. In *Metal Ions in Biological Systems*; Sigel, H., Sigel, A., Eds.; Marcel Dekker: New York, 1994; Vol. *30*, p 315. Borman, C. D.; Saysell, C. G.; Sokolowski, A.; Twitchett, M. B.; Wright, C.; Sykes, A. G. *Coord. Chem. Rev.* **1999**, *190*−*192*, 771. McPherson, M. J.; Parsons, M. R.; Spooner, R. K.; Wilmot, C. M. In *Handbook for metalloproteins*; Messerschmidt, A., Huber, R., Poulos, T., Wieghardt, K., Eds.; Wiley: New York, 2001; Vol. *2*, p 1272. Whittaker, J. W. In *Advances in Protein Chemistry*; Richards, F. M., Eisenberg, D. S., Kuriyan, J., Eds.; Academic Press/Elsevier: Amsterdam, 2002; Vol. *60*, p 1.Whittaker, J. W. *Chem. Rev.* **2003**, *103*, 2347. Rogers, M. S.; Dooley, D. M. *Curr. Opin. Chem. Biol.* **2003**, *7*, 189. Firbank, S. J.; Rogers, M.; Hurtado-Guerrero, R.; Dooley, D. M.; Halcrow, M. A.; Phillips, S. E. V.; Knowles, P. F.; McPherson, M. J. *Biochem. Soc. Trans.* **2003**, *31*, 506.

 Published on Web 12/10/2009 © 2009 American Chemical Society

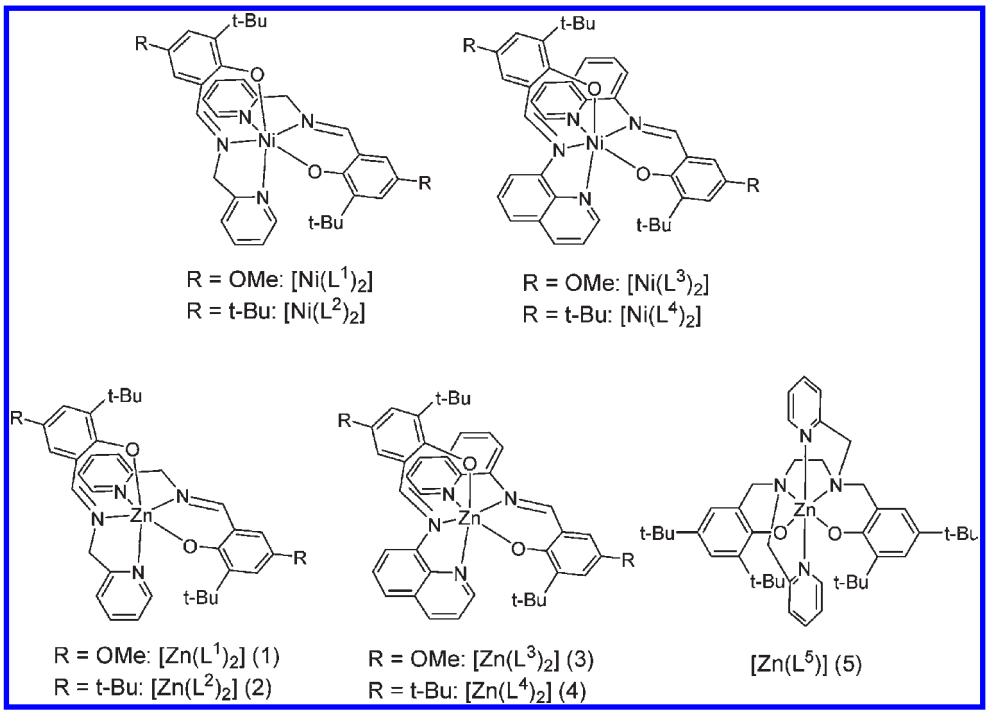

Figure 1. Ligands used in this study.

phenolates.[3] Recently we also focused our interest on square-planar bis-phenolate nickel(II) complexes of tetradentate Schiff bases.[4] We have shown that their one-electron oxidation affords a delocalized radical, i.e. the singly occupied molecular orbital (SOMO) is mainly distributed on the ligand, with a non-negligible contribution from the metal (thus giving rise to a small Ni(III) character of the complex). The phenolate para substituent features electronic properties that were shown to modulate slightly (but significantly!) the contribution of the metal orbital to the SOMO. For instance, its magnitude has been estimated by density functional theory (DFT) to 6.8% for the *tert*-butyl para substituent, whereas it is solely 1.6% for the $N(CH_3)_2$ substituent.[5] By investigating the oxidative chemistry of octahedral bis-phenolate nickel(II) complexes of tridentate Schiff bases,[6] we found that the influence of the phenolate para substituent could be dramatically enhanced. For instance, oxidation of $[Ni(L^1)_2]$ (Figure 1) is ligand-centered, affording an $S_t = {}^1/_2$ system (antiferromagnetic coupling between the high-spin Ni(II) ion and the radical spin), whereas oxidation of $[Ni(L^2)_2]$ is rather metal-centered, thus affording a Ni(III) complex. An intriguing question in this latter series is which behavior could be expected if the redox-active nickel ion is replaced by a redox-innocent ion: in other words, How does the complex behave when the oxidation is forced to be ligand-centered? We herein address this question in a series of zinc complexes isolated from the tridentate Schiff bases HL^1-HL^4 and the hexadentate Mannich base H_2L^5. We refrained from using tridentate Mannich bases in this study because of their high flexibility which may favor the existence of several isomers of the zinc complex in solution. It is noteworthy that although the geometry commonly adopted by the zinc ion is square pyramidal, we preferred this metal to other redox-innocent ones belonging to the first row because (i) it does not exhibit any nuclear spin and (ii) its formal charge is similar to that of the nickel references. As will be shown below, this choice was fortunate, since both the ligand field and the chelate effect will favor an octahedral geometry around the metal ion. The electronic structures as well as the molecular properties of the one- and two-electron-oxidized species have been explored by combined electrochemical, spectroscopic, and DFT techniques.

Results and Discussion

Preparation of the Ligands and Complexes. $HL^1-H_2L^5$ have been synthesized according to published procedures.[6−8] The zinc complexes $[Zn(L^1-L^4)_2]$ (**1**−**4**, respectively) were obtained by adding 1 molar equiv of $Zn(OAc)_2\cdot 2H_2O$ to 2 equiv of HL^1-HL^4 in MeOH in the presence of NEt_3. Single crystals of **4** were grown by slow evaporation of a saturated acetone solution.

The partially protonated zinc complex $[Zn(HL^5)]^+$ ($(\mathbf{5H})^+$), in which only one phenol is deprotonated, has been previously described by Neves et al.[8] Obviously the

(3) For reviews see: Jazdzewski, B. A.; Tolman, W. B. *Coord. Chem. Rev.* **2000**, *200*−*202*, 633–685. Krüger, H. J. *Angew. Chem., Int. Ed.* **1999**, *38*, 627. Itoh, S.; Taki, M.; Fukuzumi, S. *Coord. Chem. Rev.* **2000**, *198*, 3. Chaudhuri, P.; Wieghardt, K. *Prog. Inorg. Chem.* **2001**, *50*, 151. Chaudhuri, P.; Wieghardt, K. *Prog. Inorg. Chem.* **2001**, *50*, 151. Thomas, F. *Eur. J. Inorg. Chem.* **2007**, 2379.

(4) Rotthaus, O.; Jarjayes, O.; Thomas, F.; Philouze, C.; Perez Del Valle, C.; Saint-Aman, E.; Pierre, J. L. *Chem. Eur. J.* **2006**, *12*, 2293. Rotthaus, O.; Thomas, F.; Jarjayes, O.; Philouze, C.; Saint-Aman, E.; Pierre, J. L. *Chem. Eur. J.* **2006**, *12*, 6953. Rotthaus, O.; Jarjayes, O.; Philouze, C.; Pérez Del Valle, C; Thomas, F. *Dalton Trans.* **2009**, 1792.

(5) Rotthaus, O.; Jarjayes, O.; Perez Del Valle, C.; Philouze, C.; Thomas, F. *Chem. Commun.* **2007**, 4462.

(6) Rotthaus, O.; Labet, V.; Philouze, C.; Jarjayes, O.; Thomas, F. *Eur. J. Inorg. Chem.* **2008**, 4215.

(7) Wong, Y. L.; Yan, Y.; Chan, E. S. H.; Yang, Q.; Mak, T. C. W.; Ng, D. K. P. *J. Chem. Soc., Dalton Trans.* **1998**, 3057. Cameron, A.; Gibson, V. C.; Redshaw, C.; Segal, J. A.; White, A. J. P.; Williams, D. J. *Dalton Trans.* **2002**, 415. Imbert, C.; Hratchian, H. P.; Lanznaster, M.; Heeg, M. J.; Hryhorczuk, L. M.; McGarvey, B. R.; Schlegel, H. B.; Verani, C. N. *Inorg. Chem.* **2005**, *44*, 7414. Shakya, R.; Imbert, C.; Hratchian, H. P.; Lanznaster, M.; Heeg, M. J.; McGarvey, B. R.; Allard, M.; Schlegel, H. B.; Verani, C. N. *Dalton Trans.* **2006**, 2517.

(8) Dos Anjos, A.; Bortoluzzi, A. J.; Szpoganicz, B.; Caro, M. S. B.; Friedermann, G. R.; Mangrich, A. S.; Neves, A. *Inorg. Chim. Acta* **2005**, *358*, 3106.

Table 1. Crystallographic Data for **4** and **5**

	4	**5**·CH_3CN
formula	$C_{48}H_{54}ZnN_4O_2$	$C_{46}H_{63}ZnN_5O_2$
M_r	784.36	783.42
cryst syst	monoclinic	orthorhombic
space group	$P2_1/c$	$Pna2_1$
a/Å	15.142(1)	19.791(3)
b/Å	15.545(2)	17.329(2)
c/Å	18.131(2)	12.511(2)
α/deg	90	90
β/deg	101.23(1)	90
γ/deg	90	90
V/Å^3	4186.0(7)	4290.8(8)
Z	4	4
T/K	200	200
D_c/g cm^{-3}	1.245	1.213
μ (cm^{-1})	6.30	6.15
monochromator	graphite	graphite
wavelength (λ/Å)	Mo Kα (0.710 73)	Mo Kα (0.710 73)
no. of rflns collected	35 094	29 355
no. of indep rflns (R_{int})	9167 (0.138 94)	6706 (0.122 65)[a]
no. of obsd rflns	5692 ($I > 2\sigma(I)$)	10 689 ($I > 2\sigma(I)$)[b]
R	0.0635	0.0555
R_w	0.0680	0.0771

[a] Friedel included. [b] Friedel not merged.

Table 2. Selected Bond Lengths (Å) and Angles (deg) for **4** and **5**

Compound **4**

Zn−O1	2.019(2)	Zn−N3	2.103(3)
Zn−N2	2.238(3)	Zn−N1	2.104(3)
Zn−O2	1.997(2)	Zn−N4	2.173(3)
O1−Zn−O2	92.57(9)	N1−Zn−N3	166.9(1)
O1−Zn−N3	103.0(1)	N2−Zn−N4	87.3(1)
O2−Zn−N2	92.8(1)	O1−Zn−N2	163.8(1)
N1−Zn−N2	76.2(1)	O2−Zn−N1	98.3(1)
N2−Zn−N3	92.4(1)	O2−Zn−N4	165.3(1)
O1−Zn−N1	87.94(9)	N1−Zn−N4	95.9(1)
O1−Zn−N4	91.30(9)	N3−Zn−N4	76.8(1)
O2−Zn−N3	88.51(9)		

Compound **5**

Zn−O1	1.985(2)	Zn−N3	2.233(2)
Zn−N2	2.280(2)	Zn−N1	2.246(2)
Zn−O2	2.002(2)	Zn−N4	2.266(2)
O1−Zn−O2	106.08(8)	N1−Zn−N3	75.14(8)
O1−Zn−N3	89.21(9)	N2−Zn−N4	74.81(8)
O2−Zn−N2	90.08(8)	O1−Zn−N2	156.07(8)
N1−Zn−N2	78.74(8)	O2−Zn−N1	153.46(8)
N2−Zn−N3	109.71(8)	O2−Zn−N4	94.97(8)
O1−Zn−N1	92.77(8)	N1−Zn−N4	104.99(8)
O1−Zn−N4	86.09(9)	N3−Zn−N4	175.31(9)
O2−Zn−N3	86.40(8)		

acetate base used in the synthesis is not strong enough to deprotonate the second phenol. In order to obtain a bis-phenolate complex, we have used an excess of NEt_3 during the synthesis and recrystallized it by slow evaporation of CH_3CN. In this way the fully deprotonated complex [Zn(L^5)] (**5**) could be obtained as colorless single crystals.

Structures of the Zn(II) Complexes 4 and 5. The crystallographic data for **4** and **5** are reported in Table 1, and selected bond distances and angles are given in Table 2. **4** contains a zinc(II) ion within a pseudo-octahedral environment (Figure 2), chelated by two fully deprotonated ligands. The metal is coordinated by two nitrogen atoms from two quinolines (N(2) and N(4)) and two imines (N(1) and N(3)), as well as two oxygens O(1) and O(2) from the phenolate groups. The two ligands are arranged in a meridional fashion, with a cis orientation of the phenolate moieties (the angle O(1)−Zn−O(2) is 92.57(9)°). As observed in the analogous nickel complex, the imine nitrogens are trans to one another (N(1)−Zn−N(3) angle of 166.9(1)°), whereas the pyridine nitrogens are cis to one another (N(2)−Zn−N(4) angle of 87.3(1)°). A similar arrangement is expected for **1**−**3**, the fac orientation of the ligands being unfavored in related complexes.[6,9]

The Zn−O(1) and Zn−O(2) bond lengths in **4** are inequivalent, with values of 2.019(2) and 1.997(2) Å, respectively, and are remarkably similar to the Ni−O(1) and Ni−O(2) distances in [Ni(L^2)$_2$] and [Ni(L^4)$_2$]. As expected, the Zn−N bond distances are longer, with the Zn−N_{imine} bond distances Zn−N(1) and Zn−N(3) being 2.104(3) and 2.103(3) Å and the Zn−$N_{quinoline}$ bond distances Zn−N(2) and Zn−N(4) being 2.238(3) and 2.173(3) Å, respectively. A comparison between **4** and the nickel complex [Ni(L^4)$_2$] reveals that the M−$N_{quinoline}$ bond distances are significantly longer in the former case and, consequently, that these bonds are much weaker.

Spectroscopic Properties of the Complexes. The UV−vis spectra of **1**−**5** are depicted in Figure 3, and data are given in Table 3. The spectra of **1** and **2** consist of intense transitions at 360, 415 nm and at 333, 390 nm, respectively. The contribution of the salicylidene π orbitals to these transitions is evident through the shift of λ_{max} according to the electronic properties of the phenolate substituent. A similar behavior is observed for **3** and **4**, although the transitions are observed at lower energies (496 and 476 nm, respectively), as expected for an extended conjugation over the quinoline rings. The spectrum of **5** displays a strong absorption band at 304 nm (ε = 8160 M^{-1} cm^{-1}) attributed to a phenolate π−π* transition. The fact that the zinc complex of H_2L^5 has been previously reported only in a partially protonated form stimulated us to examine its behavior in the presence of base and acid. Upon addition of $HClO_4$ the phenolate π−π* band shifts toward shorter wavelengths (Figure S1; Supporting Information), whereas addition of NEt_3 did not result in significant changes. The shift of λ_{max} toward shorter wavelengths is attributed to the successive protonation of the phenolate moieties.[10] The π−π* transition of the phenolate is only observed as a shoulder at ca. 300 nm (ε = 3870 M^{-1} cm^{-1}) at 1 equiv of $HClO_4$ added, whereas it is absent at 2 equiv of $HClO_4$ added and is replaced by the phenol π−π* transition at 269 nm (ε = 6700 M^{-1} cm^{-1}).

Electrochemistry. The electrochemical behavior of **1**−**5** has been studied in CH_2Cl_2 by cyclic voltammetry (CV), differential pulse voltammetry (DPV), and rotating-disk electrode (RDE) voltammetry. All the potential values are given relative to the Fc/Fc$^+$ reference electrode.

The CV curves of **1**−**5** exhibit two reversible oxidation waves (Figure 4 and Table 4). Each redox process corresponds to a one-electron transfer, as judged by

(9) Imbert, C.; Hratchian, H. P.; Lanznaster, M.; Heeg, M. J.; Hryhorczuk, L. M.; McGarvey, B. R.; Schlegel, H. B.; Verani, C. N. *Inorg. Chem.* **2005**, *44*, 7414.

(10) See electronic supplementary information in: Michel, F.; Thomas, F.; Hamman, S.; Saint-Aman, E.; Bucher, C.; Pierre, J.-L. *Chem. Eur. J.* **2004**, *10*, 4115.

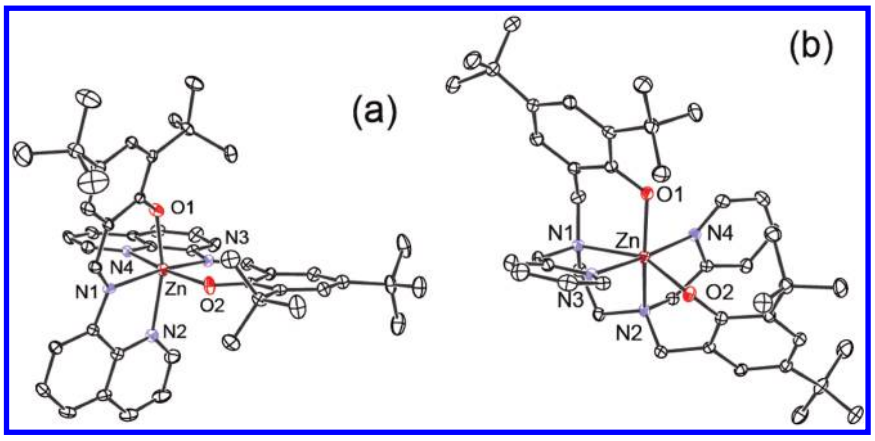

Figure 2. X-ray crystal structures of **4** (a) and **5** (b) shown with 30% thermal ellipsoids.

coulometric titration and rotating disk electrode (RDE) amperometric titration. The potential values are $E_{1/2}{}^1 = -0.072$ V and $E_{1/2}{}^2 = 0.141$ V for **1** and $E_{1/2}{}^1 = 0.084$ V and $E_{1/2}{}^2 = 0.336$ V for **2**. The higher values obtained for **2** result from the lower electron-donating properties of the *tert*-butyl relative to the methoxyl group, thus confirming the participation of the ligand in the oxidation process. The redox waves thus correspond to the successive formation of mono- and diradical species. As a comparison, the $E_{1/2}{}^1$ values obtained for the nickel analogues $[Ni(L^1)_2]$ and $[Ni(L^2)_2]$ are slightly lower: −0.17 and −0.01 V, respectively.[6] Interestingly the difference $\Delta E_{1/2}{}^1 = E_{1/2}{}^1(\text{zinc}) - E_{1/2}{}^1(\text{nickel})$ is ca. 0.1 V for both $[M(L^1)_2]$ and $[M(L^2)_2]$. This analogy is remarkable, as one-electron oxidation of $[Ni^{II}(L^1)_2]$ affords a radical, whereas one-electron oxidation of $[Ni^{II}(L^2)_2]$ affords a Ni(III) complex. This similarity of $\Delta E_{1/2}$ thus suggests that the initial electron transfer in the two nickel complexes occurs on the ligand. When the phenoxyl para substituent is the least electron-donating *tert*-butyl group, subsequent electron transfer from the metal to the ligand occurs, giving rise to a Ni(III) complex. It is noticeable that the same behavior is observed for **3** and **4** (although these complexes are slightly harder to oxidize).

5 also exhibits two one-electron redox waves at $E_{1/2}{}^1 = -0.036$ V and $E_{1/2}{}^2 = 0.232$ V, each corresponding to the oxidation of one phenolate into a phenoxyl radical. These values are slightly lower than for the Schiff base complexes **2** and **4**, for which the conjugated imine exerts an electron-withdrawing inductive effect. It is instructive to compare these potentials with those reported for the zinc bis-phenolate complex of a pentadentate Mannich base, 1-ethyl-4,7-bis(3-*tert*-butyl-5-methoxy-2-hydroxybenzyl)-1,4,7-triazacyclononane, and the partially protonated species $(\mathbf{5H})^+$. The former complex exhibits oxidation potentials that are slightly lower ($E_{1/2}{}^1 = -0.10$ V and $E_{1/2}{}^2 = 0.15$ V), in agreement with the enhanced electron-donating properties of the methoxy substituent.[11] The latter exhibits a single oxidation wave, since only one phenol is deprotonated and thus oxidizable. It is observed at the much higher value $E_{1/2} = 0.390$ V,[8] which is ascribed to the additional positive charge of $(\mathbf{5H})^+$ compared to **5**. It is also noticeable that the redox potentials obtained for **5** are very close to those obtained for **1** and **3**, thus showing that replacement of the imine by an aminomethyl group counterbalances efficiently the lower electron-donating properties of the *tert*-butyl vs methoxyl substituent, as observed in the nickel analogues.

One- and Two-Electron-Oxidized Complexes. The one- and two-electron-oxidized complexes have been generated by bulk electrolysis of ca. 0.7 mM CH_2Cl_2 (+0.1 M TBAP) solutions of each compound at 233 K. The amount of oxidized species was monitored by both coulometric and RDE amperometric titration.

The UV−vis spectra of the electrolytic solutions at one and two electrons removed (formation of the mono- and dication, respectively) are depicted in Figure 3. Upon electrolysis the yellow solutions of **1** and **2** turned dark green and the orange-red solutions of **3** and **4** turned brown, whereas the colorless solution of **5** turned green. The UV−vis spectrum of **1** in its oxidized form differs significantly from that of the initial compound. It is characterized by sharp and intense absorptions at 420 and 444 nm and a lower intensity band at around 600 nm, all being typical for $\pi-\pi^*$ transitions of phenoxyl radicals.[12] Oxidation to the dication $(\mathbf{1}^{\bullet\bullet})^{2+}$ results in further sharpening of these bands and an increase in their intensity, thus confirming the formation of a bis-phenoxyl radical species according to

$$\mathbf{1} \rightleftharpoons (\mathbf{1}^{\bullet})^{+} \rightleftharpoons (\mathbf{1}^{\bullet\bullet})^{2+}$$

Similarly, oxidation of **2** into $(\mathbf{2}^{\bullet})^{+}$ and $(\mathbf{2}^{\bullet\bullet})^{2+}$ is accompanied by the appearance of strong $\pi-\pi^*$ transitions of phenoxyl radicals at around 400 and 420 nm, together with a broad and less intense band at around 750 nm. The shift of λ_{max} toward lower wavelengths compared to $(\mathbf{1}^{\bullet})^{+}$ and $(\mathbf{1}^{\bullet\bullet})^{2+}$ results from the lower electron-donating properties of the phenoxyl para substituent.[13]

(11) Bill, E.; Müller, J.; Weyhermüller, T.; Wieghardt, K. *Inorg. Chem.* **1999**, *38*, 5795.

(12) Chang, H. M.; Jaffe, H. H. *Chem. Phys. Lett.* **1973**, *23*, 146. Chang, H. M.; Jaffe, H. H.; Masmandis, C. A. *J. Phys. Chem.* **1975**, *79*, 1118. Johnston, L. J.; Mathivanan, N.; Negri, F.; Siebrand, W.; Zerbetto, F. *Can. J. Chem.* **1993**, *71*, 1655. Takahashi, J.; Shida, T. *Bull. Chem. Soc. Jpn.* **1994**, *67*, 2038. Takahashi, J.; Momose, T.; Shida, T. *Bull. Chem. Soc. Jpn.* **1994**, *67*, 964. Liu, R.; Morokuma, K.; Mebel, A. M.; Lin, M. C. *J. Phys. Chem.* **1996**, *100*, 9314. Hinchliffe, A.; Steinbank, R. E.; Ali, M. A. *Theor. Chim. Acta* **1996**, *5*, 95. Radziszewski, J. G.; Gil, M.; Gorski, A.; Spanget-Larsen, J.; Waluk, J.; Mroz, B. J. *J. Chem. Phys.* **2001**, *115*, 9733.

(13) Philibert, A.; Thomas, F.; Philouze, C.; Hamman, S.; Saint-Aman, E.; Pierre, J.-L. *Chem. Eur. J.* **2003**, *9*, 3803.

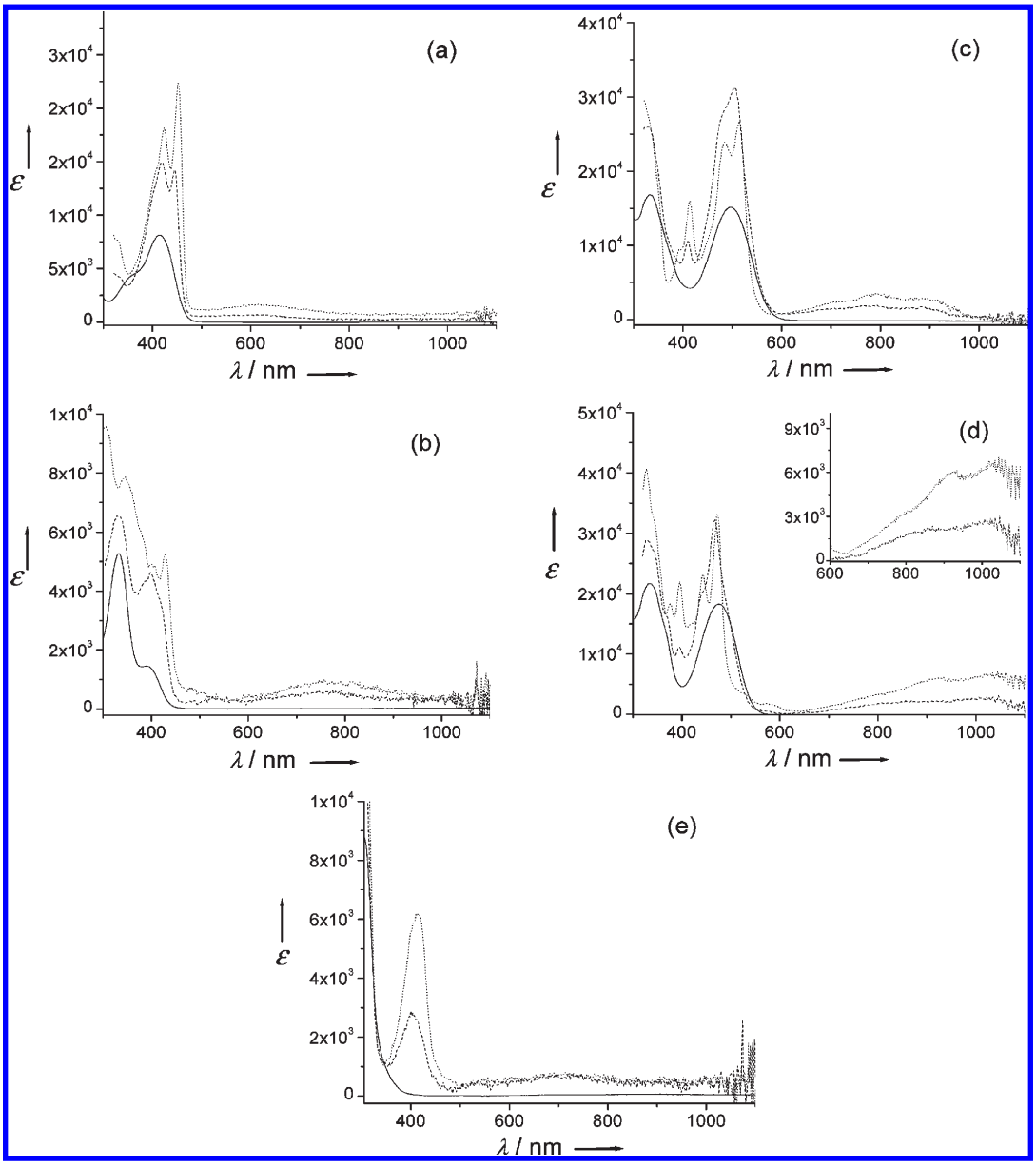

Figure 3. Electronic spectra of CH_2Cl_2 solutions (+0.01 M TBAP) of the neutral (298 K) and electrogenerated mono- and dications (235 K): (a) **1** (solid line), $(\mathbf{1}^{\bullet})^{+}$ (dashed line), and $(\mathbf{1}^{\bullet\bullet})^{2+}$ (dotted line); (b) **2** (solid line), $(\mathbf{2}^{\bullet})^{+}$ (dashed line), and $(\mathbf{2}^{\bullet\bullet})^{2+}$ (dotted line); (c) **3** (solid line), $(\mathbf{3}^{\bullet})^{+}$ (dashed line), and $(\mathbf{3}^{\bullet\bullet})^{2+}$ (dotted line); (d) **4** (solid line), $(\mathbf{4}^{\bullet})^{+}$ (dashed line), and $(\mathbf{4}^{\bullet\bullet})^{2+}$ (dotted line) (the insert represents a zoom of the near-IR region); (e) **5** (solid line), $(\mathbf{5}^{\bullet})^{+}$ (dashed line), and $(\mathbf{5}^{\bullet\bullet})^{2+}$ (dotted line). The path length is 1.000 cm.

The UV−vis spectra obtained upon one- and two-electron oxidation of **3** are much more rich with the development of transitions at ca. 390, 410, 480, and 510 nm and with broad absorptions at 800 and 900 nm. These new absorptions are slightly shifted in the one- and two-electron-oxidized forms of **4**, as they are observed at ca. 380, 390, 440, and 470 nm, the broad absorptions being observed at 900 and 1000 nm. The intensity of the latter absorption is remarkable, with molar extinction coefficients of 1650 M^{-1} cm^{-1} for $(\mathbf{3}^{\bullet})^{+}$ and 2650 M^{-1} cm^{-1} for $(\mathbf{4}^{\bullet})^{+}$. Such near-IR absorptions have been reported for *o*-benzoiminosemiquinonate complexes[14] and some one-electron-oxidized bis-salicylidene complexes and attributed to intramolecular phenolate−phenoxyl charge transfers.[15] Preliminary TD-DFT calculations on $(\mathbf{3}^{\bullet})^{+}$ and $(\mathbf{4}^{\bullet})^{+}$ also suggest that this near-IR transition arises from an intramolecular charge transfer (see below).[16]

The electronic spectrum of $(\mathbf{5}^{\bullet})^{+}$ is characterized by phenoxyl radical $\pi-\pi^*$ transitions at 402 and 414 nm, with a broad absorption band at around 700 nm. These features are similar to those reported by Shimazaki et al. for the zinc−phenoxyl complex of a tetradentate tripodal

(14) Chaudhuri, P.; Verani, C. N.; Bill, E.; Bothe, E.; Weyhermüller, T.; Wieghardt, K. *J. Am. Chem. Soc.* **2001**, *123*, 2213. Min, K. S.; Weyhermüller, T.; Bothe, E.; Wieghardt, K. *Inorg. Chem.* **2004**, *43*, 2922.

(15) Pratt, R. C.; Stack, T. D. P. *J. Am. Chem. Soc.* **2003**, *125*, 8716.

(16) The one-electron-oxidized nickel analogue of $(\mathbf{3}^{\bullet})^{+}$ has been identified as the radical complex $[Ni^{II}(L^3)(L^3)^{\bullet}]^{+}$, whereas the nickel analogue of $(\mathbf{4}^{\bullet})^{+}$ is the Ni(III) species $[Ni^{III}(L^4)_2]^{+}$.[6] In agreement with this, the sharp typical $\pi-\pi^*$ phenoxyl transition at ca. 400−420 nm that is widely used as a diagnostic for the presence of a phenoxyl species is observed for the three radical compounds $(\mathbf{3}^{\bullet})^{+}$, $(\mathbf{4}^{\bullet})^{+}$, and $[Ni^{II}(L^3)(L^3)^{\bullet}]^{+}$, whereas it is absent in the optical spectrum of $[Ni^{III}(L^4)_2]^{+}$. The spectra of $[Ni^{II}(L^1)(L^1)^{\bullet}]^{+}$ and $[Ni^{III}(L^2)_2]^{+}$ are not resolved enough to observe such differences.

Table 3. UV−Vis Properties[a] of the Zinc Complexes

complex	λ_{max}/nm (ε/M^{-1} cm^{-1})
1	360 sh (4420), 415 (8120)
$(\mathbf{1}^{\bullet})^{+}$	420 (14 660), 444 (14 200), 605 br (650)
$(\mathbf{1}^{\bullet\bullet})^{2+}$	424 (18 150), 452 (22 340), 622 br (1570)
2	333 (5270), 390 (1450)
$(\mathbf{2}^{\bullet})^{+}$	332 (6530), 398 (4630), 422 sh (3410), 750 br (560)
$(\mathbf{2}^{\bullet\bullet})^{2+}$	346 (7860), 402 (4910), 428 (5250), 750 br (950)
3	333 (16 820), 496 (15 140)
$(\mathbf{3}^{\bullet})^{+}$	410 (10 540), 480 sh (27 650), 504 (31 030), 680 br (1330), 780 br (1700), 890 br (1650)
$(\mathbf{3}^{\bullet\bullet})^{2+}$	392 (9460), 414 (16 010), 484 (23 970), 514 (26 730), 700 br (2300), 800 br (3260), 890 br (2800)
4	333 (21 720), 476 (18 280)
$(\mathbf{4}^{\bullet})^{+}$	380 sh (11 020), 394 (11 070), 442 sh (20 250), 468 (32 240), 850 br (2200), 1010 br (2650)
$(\mathbf{4}^{\bullet\bullet})^{2+}$	376 (18 300), 396 (22 020), 444 (23 220), 472 (33 260), 528 sh (3480), 582 sh (1640), 780 br (2900), 920 br (6000), 1020 br (6700)
5	304 (8160)
$(\mathbf{5}^{\bullet})^{+}$	402 (2720), 414 sh (2550), 700 br (630)
$(\mathbf{5}^{\bullet\bullet})^{2+}$	402 sh (5600), 414 (6170), 700 br (725)

[a] In CH_2Cl_2 (+5 mM TBAP) at 235 K.

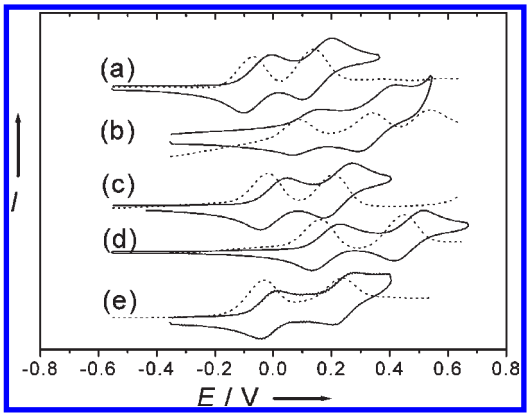

Figure 4. Electrochemical behavior of 0.7 mM CH_2Cl_2 solutions (+0.1 M TBAP) of (a) **1**, (b) **2**, (c) **3**, (d) **4**, and (e) **5**: (solid lines) CV curves at a scan rate of 0.1 V s^{-1}; (dotted lines) DPV curves at a pulse width of 0.05 s, amplitude of 0.05 V, and period of 0.2 s (T = 298 K, reference Fc/Fc^{+}).

Table 4. Electrochemical Properties[a] of Complexes **1**−**5**

	$E_{1/2}$/V	
complex		
1	−0.072	0.141
2	0.084	0.336
3	−0.024	0.203
4	0.156	0.444
5	−0.036	0.232
5H	0.39[b]	

[a] Potential values given vs the Fc/Fc^{+} reference electrode, *at* T = 298 K; complex concentrations are 0.7−1 mM. $E_{1/2}$ values were obtained from DPV measurements by adding half of the pulse amplitude to the E_p value. The confidence level is ±0.005 V. [b] From ref 8.

ligand related to H_2L.[5,17] The fact that the intensity of the former bands is almost twice as large in $(\mathbf{5}^{\bullet\bullet})^{2+}$ compared to $(\mathbf{5}^{\bullet})^{+}$ suggests that the phenoxyl moieties of $(\mathbf{5}^{\bullet\bullet})^{2+}$ are the least electronically coupled in the series.

(17) Shimazaki, Y.; Yajima, T.; Shiraiwa, T.; Yamauchi, O. *Inorg. Chim. Acta* **2009**, *362*, 2467.

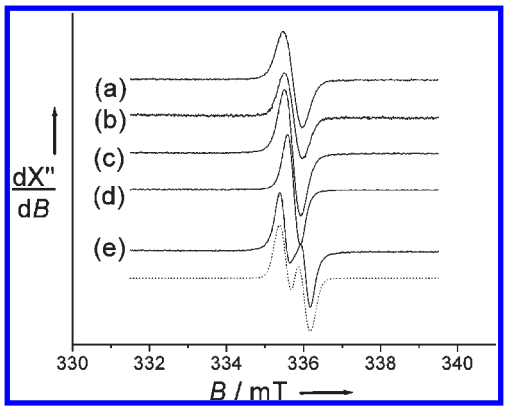

Figure 5. X-Band EPR spectra (solid lines) of 0.7 mM CH_2Cl_2 solutions: (a) $(\mathbf{1}^{\bullet})^{+}$; (b) $(\mathbf{2}^{\bullet})^{+}$; (c) $(\mathbf{3}^{\bullet})^{+}$; (d) $(\mathbf{4}^{\bullet})^{+}$; (e) $(\mathbf{5}^{\bullet})^{+}$. Dotted lines represent a simulation using the parameters given in the text. Conditions: frequency, 9.42 GHz; power, 20 mW; modulation frequency, 100 kHz; amplitude, 0.0099 mT (a, c, d) or 0.0312 mT (b, e); T = 233 K.

The stability of the monoradical species has been evaluated by monitoring the disappearance of the phenoxyl $\pi-\pi^*$ transition as a function of time at 298 K. $(\mathbf{1}^{\bullet})^{+}$ decomposes in a first-order process, with a half-life of 5 min (k_{dec} = 0.142 min^{-1}). Decomposition of $(\mathbf{2}^{\bullet})^{+}$ occurs faster, the half-life of $(\mathbf{2}^{\bullet})^{+}$ being less than 1 min. These results could be correlated to the lower redox potential of **1** relative to **2**, the methoxy para substituent giving rise to more stable phenoxyl radical species. While $(\mathbf{1}^{\bullet})^{+}$ and $(\mathbf{2}^{\bullet})^{+}$ decompose within the minute time scale, the half-life of $(\mathbf{4}^{\bullet})^{+}$ is found to be 92 min (k_{dec} = 7.55 × 10^{-3} min^{-1}). $(\mathbf{3}^{\bullet})^{+}$ exhibits a remarkable stability, as only minor changes are observed in its spectrum after 15 h at 298 K. This radical is the most stable of the series (it is also one of the most stable Zn−phenoxyl radical species reported), despite the fact that the phenoxyl/phenolate redox couple of **3** is not the lowest one. This fact is ascribed to the increased delocalization of the charge within the quinoline with respect to the pyridine group.

$(\mathbf{5}^{\bullet})^{+}$ was found to be poorly stable, with a half-life of less than 1 min at 298 K. The rate constant reported for the self-decomposition of $(\mathbf{5H}^{\bullet})^{2+}$ is 0.306 min^{-1} (half-life of ca. 2 min),[8] thus showing that the weak delocalization of the spin density over the other phenolate surprisingly does not contribute to the stabilization of the radical species in this case.

EPR Spectroscopy. The 233 K EPR spectra of CH_2Cl_2 solutions of the monoradical species $(\mathbf{1}^{\bullet})^{+}$−$(\mathbf{5}^{\bullet})^{+}$ are shown in Figure 5, and data are given in Table 5. The spectra of $(\mathbf{1}^{\bullet})^{+}$−$(\mathbf{4}^{\bullet})^{+}$ consist of an unresolved isotropic signal centered at g = 2.005 whose line width is ca. 0.5 mT (peak-to-peak). Interestingly, the signal observed for $(\mathbf{3}^{\bullet})^{+}$ is broader than that of $(\mathbf{4}^{\bullet})^{+}$. This likely results from additional interaction of the electron spin with the three hydrogens of the methoxy group. This difference is not so clear when $(\mathbf{1}^{\bullet})^{+}$ is compared to $(\mathbf{2}^{\bullet})^{+}$, presumably due to additional line broadening.

The spectrum of $(\mathbf{5}^{\bullet})^{+}$ differs significantly from those of $(\mathbf{1}^{\bullet})^{+}$−$(\mathbf{4}^{\bullet})^{+}$. It consists of a doublet which arises from the interaction of the electron spin with one hydrogen nucleus (I_H = $^1/_2$). The hyperfine coupling constant obtained from simulation is relatively large (0.44 mT), in spite of

Table 5. EPR Properties of the Mono- and Diradical Complexes of **1**−**5**

	monoradical ($S = {}^1/_2$)		diradical ($S = 1$)	
complex	g	line width[a]	exptl D	exptl E/D
1	2.0052	0.50	−0.0163	0
2	2.0051	0.48	−0.0182	0
3	2.0051	0.43	−0.0144	0
4	2.0051	0.34	−0.0160	0
5	2.0050	$A_H = 0.44$[b]	−0.0115	0

[a] Peak to peak. [b] The hyperfine coupling constant with one benzylic hydrogen is given.

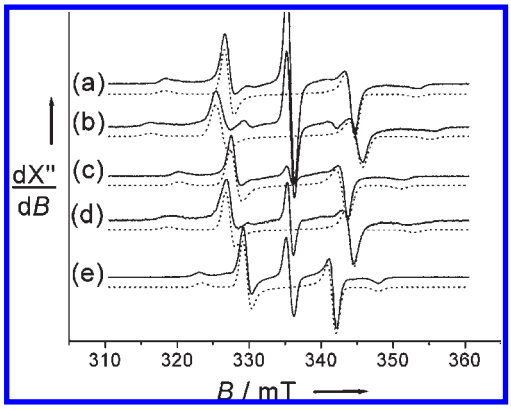

Figure 6. X-Band EPR spectra (solid lines) of 0.7 mM CH_2Cl_2 solutions: (a) $(\mathbf{1}^{\bullet\bullet})^{2+}$; (b) $(\mathbf{2}^{\bullet\bullet})^{2+}$; (c) $(\mathbf{3}^{\bullet\bullet})^{2+}$; (d) $(\mathbf{4}^{\bullet\bullet})^{2+}$; (e) $(\mathbf{5}^{\bullet\bullet})^{2+}$. Dotted lines represent simulations using the parameters given in the text. Conditions: frequency, 9.42 GHz; power, 20 mW; modulation frequency, 100 kHz; amplitude, 0.039 mT (a), 0.078 mT (b), 0.011 mT (c, d), 0.078 mT (e); T = 100 K.

the absence of hydrogen atom at the ortho and para positions of the phenoxyl. Examination of the X-ray crystal structure of **5** reveals that one of the benzylic hydrogens (H3) is significantly out of the phenolate ring plane formed by C1−C6, the C1−C6−C7−H3 torsion angle being ca. 52° (C7 is the benzylic carbon, C1 and C6 two adjacent carbons located within the phenolate ring). By considering that the six-membered coordination ring −[Zn−O1−C1−C6−C7−N1]− is conformationally rigid, H3 is expected to interact strongly with the unpaired spin density, resulting in a large hfc constant, as observed experimentally. This further confirms that the radical remains coordinated to the zinc ion in $(\mathbf{5}^{\bullet})^{+}$.[11,18]

The X-band EPR spectra of $(\mathbf{1}^{\bullet\bullet})^{2+}$−$(\mathbf{5}^{\bullet\bullet})^{2+}$ recorded at 100 K (Figure 6) consist of a five-line pattern centered at $g \approx 2.005$. The intensity of the central line relative to the outer signals varies according to the sample preparation, thus suggesting that this signature cannot correspond to a single diradical species. We therefore attribute the central line to a contaminant monoradical species and the dominant symmetric outer peaks to spin triplet resonances. Examination of the low-field region reveals the presence of a forbidden half-field transition $\Delta M_S = \pm 2$ at $g = 4$, further confirming this assumption. The zero-field splitting (ZFS) parameters were obtained from simulation. While all the systems were found to be axial (within experimental error), i.e. $E = 0$ cm^{-1}, the $|D|$ value was

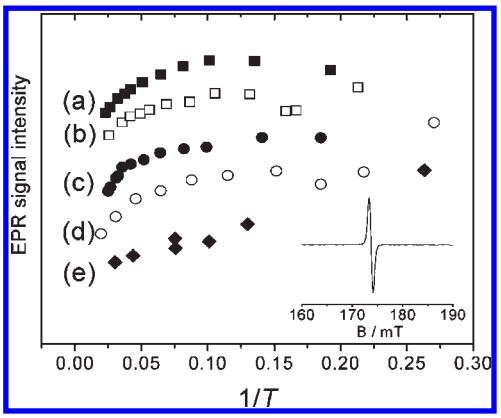

Figure 7. Curie plots for (a) $(\mathbf{1}^{\bullet\bullet})^{2+}$, (b) $(\mathbf{2}^{\bullet\bullet})^{2+}$, (c) $(\mathbf{3}^{\bullet\bullet})^{2+}$, (d) $(\mathbf{4}^{\bullet\bullet})^{2+}$, and (e) $(\mathbf{5}^{\bullet\bullet})^{2+}$. The insert represents the low-field region of the EPR spectrum of $(\mathbf{5}^{\bullet\bullet})^{2+}$. Conditions: frequency, 9.74 GHz; power, 10 mW; modulation frequency, 100 kHz; amplitude, 0.4 mT; T = 9.9 K.

found to depend signicantly on the ligand structure. It is 0.0163 cm^{-1} for $(\mathbf{1}^{\bullet\bullet})^{2+}$, 0.0182 cm^{-1} for $(\mathbf{2}^{\bullet\bullet})^{2+}$, 0.0144 cm^{-1} for $(\mathbf{3}^{\bullet\bullet})^{2+}$, 0.0160 cm^{-1} for $(\mathbf{4}^{\bullet\bullet})^{2+}$, and 0.0115 cm^{-1} for $(\mathbf{5}^{\bullet\bullet})^{2+}$. These values are much higher than those reported for uncoordinated bis H-bonded phenoxyl radicals obtained from salen ligands,[19] thus suggesting that the radicals are coordinated in $(\mathbf{1}^{\bullet\bullet})^{2+}$−$(\mathbf{5}^{\bullet\bullet})^{2+}$. The difference in D between $(\mathbf{1}^{\bullet\bullet})^{2+}$ and $(\mathbf{2}^{\bullet\bullet})^{2+}$, as well as between $(\mathbf{3}^{\bullet\bullet})^{2+}$ and $(\mathbf{4}^{\bullet\bullet})^{2+}$, is a direct effect of the substituent on the spin distribution, as the distance between the phenoxyl oxygens is not expected to vary significantly within the series. Similarly, the extended conjugation over the quinoline ring may also modify the spin distribution within the complexes and consequently affect the D value, which is experimentally observed.

The temperature dependence of the spin triplet has been examined in the 5−50 K range, and a plot of intensity (I) as a function of $1/T$ is shown in Figure 7. The deviation from linearity obtained for $(\mathbf{1}^{\bullet\bullet})^{2+}$, $(\mathbf{2}^{\bullet\bullet})^{2+}$, $(\mathbf{3}^{\bullet\bullet})^{2+}$, and $(\mathbf{4}^{\bullet\bullet})^{2+}$ reveals an excited state for the triplet. The spins in these diradicals are thus *antiferromagnetically* exchange-coupled, and the ground state is diamagnetic. From the fit of IT as a function of T with eq 1 exchange coupling constants J of -4.5 ± 1, -5.1 ± 1, -5.4 ± 2, and -4.2 ± 2 cm^{-1} were obtained for $(\mathbf{1}^{\bullet\bullet})^{2+}$, $(\mathbf{2}^{\bullet\bullet})^{2+}$, $(\mathbf{3}^{\bullet\bullet})^{2+}$, and $(\mathbf{4}^{\bullet\bullet})^{2+}$, respectively (Figures S2−S5; Supporting Information). Although these J values are larger than the energy quantum of the X-band EPR (thus confirming that our treatment of the triplet as isolated is correct), they are relatively low, in agreement with a very weak antiferromagnetic coupling.

$$IT = C \exp(2J/kT)/(1 + 3 \exp(2J/kT)) \qquad (1)$$

The situation observed for $(\mathbf{5}^{\bullet\bullet})^{2+}$ contrasts sharply with that encountered for $(\mathbf{1}^{\bullet\bullet})^{2+}$−$(\mathbf{4}^{\bullet\bullet})^{2+}$, as the plot of I as a function of $1/T$ gives a straight line. This shows that the triplet does not represent an excited but a ground state for $(\mathbf{5}^{\bullet\bullet})^{2+}$: in other words, the two spins are *ferromagnetically* exchange-coupled. This ground state is remarkable, as in zinc diradical complexes involving tetradentate Schiff bases[20] or the pentadentate Mannich base

(18) Itoh, S.; Taki, M.; Kumei, H.; Takayama, S.; Nagatomo, S.; Kitagawa, T.; Sakurada, N.; Arakawa, R.; Fukuzumi, S. *Inorg. Chem.* **2000**, *39*, 3708. Thomas, F.; Gellon, G.; Gautier-Luneau, I.; Saint-Aman, E.; Pierre, J. L. *Angew. Chem., Int. Ed.* **2002**, *41*, 3047.

(19) Thomas, F.; Jarjayes, O.; Duboc, C.; Philouze, C.; Saint-Aman, E.; Pierre, J.-L. *Dalton Trans.* **2004**, 2662.

Table 6. Calculated Coordination-Sphere Bond Lengths (Å) in Neutral and Diradical Complexes of **1**−**5** and Comparison with Experiment[a]

complex	Zn−O1	Zn−O2	Zn−N1[b]	Zn−N2[c]	Zn−N3[b]	Zn−N4[c]
1	2.058	2.056	2.114	2.332	2.120	2.282
$(\mathbf{1}^{\bullet\bullet})^{2+}$	2.150	2.151	2.144	2.176	2.143	2.175
2	2.063	2.050	2.122	2.330	2.115	2.330
$(\mathbf{2}^{\bullet\bullet})^{2+}$	2.165	2.156	2.142	2.173	2.139	2.160
3	2.069	2.067	2.141	2.257	2.142	2.257
$(\mathbf{3}^{\bullet\bullet})^{2+}$	2.131	2.128	2.169	2.160	2.169	2.158
4	2.073	2.059	2.142	2.266	2.141	2.223
	2.019(*2*)	*1.997*(*2*)	*2.104*(*3*)	*2.238*(*3*)	*2.103*(*3*)	*2.173*(*3*)
$(\mathbf{4}^{\bullet\bullet})^{2+}$	2.132	2.128	2.169	2.161	2.169	2.158
5	2.006	2.005	2.309	2.237	2.310	2.236
	1.985(*2*)	*2.002*(*2*)	*2.246*(*3*)	*2.233*(*3*)	*2.280*(*3*)	*2.266*(*3*)
$(\mathbf{5}^{\bullet\bullet})^{2+}$	2.124	2.124	2.247	2.164	2.248	2.166

[a] Average experimental values are given in italics with standard deviations in parentheses. [b] Imino/amino nitrogen atoms. [c] Pyridine/quinoline nitrogen atoms.

1-ethyl-4,7-bis(3-*tert*-butyl-5-methoxy-2-hydroxybenzyl)-1,4,7-triazacyclononane[12] the radical spins are usually *antiferromagnetically* exchanged coupled. Such ferromagnetic interactions are commonly observed in zinc complexes of *o*-iminobenzosemiquinone diradicals[21] (when the spins are not essentially uncoupled).[22] The particular behavior observed for $(\mathbf{5}^{\bullet\bullet})^{2+}$ likely does not originate solely from the imino to amino substitution but also from geometrical reasons, as will be shown below.

DFT Calculations. Geometries of the Neutral and Diradical Species. Selected structural parameters for the five complexes under consideration are given in Table 6 for both neutral and diradical systems. We first examine the optimized geometries of complexes **4** and **5**, for which experimental X-ray structures were determined. In the case of complex **5**, we observe that metal−oxygen distances are in good agreement with experiment with a maximum deviation of 0.02 Å, whereas the calculated metal−nitrogen bond lengths tend to be overestimated by up to 0.06 Å. This latter deviation was expected,[25,26] since it is well-known that weak metal−ligand bonds (such as bonds to neutral amines) are predicted with less accuracy by DFT methods in comparison to stronger metal−ligand bonds (such as bonds to O^{2-}).[23,24] Although for complex **4** the optimized metal−ligand distances are longer when compared to X-ray data, our calculations nicely reproduce some qualitative features. For instance, the optimized $Zn-N_{imine}$ distances are predicted to be shorter than the corresponding $Zn-N_{quinoline/pyridine}$ distances and our results also show an inequivalence of the two metal−oxygen bond lengths, in agreement with experimental data.[11] Comparing now the optimized structures of the neutral complexes of **1**−**5** with the corresponding diradical species $(\mathbf{1}^{\bullet\bullet})^{2+}$−$(\mathbf{5}^{\bullet\bullet})^{2+}$, we notice that all metal−oxygen distances are elongated upon oxidation by 0.09 Å on average, whereas a mean shortening of 0.11 Å occurs for the metal−nitrogen bonds involving pyridine or quinoline ligands. When inspecting the C−C and C−N bond distances within these rings, we did not observe any significant modification arising from oxidation. We thus conclude that the shortening of the $Zn-N_{quinoline/pyridine}$ bonds in the diradical systems is due to geometrical rearrangement upon oxidation. With regard now to the Zn−O distances, the situation is quite different, since the observed elongation is accompanied by a mean contraction of 0.03 Å of the C−O(hydroxyl) distances. Moreover, upon oxidation of complexes **1** and **3** the C−O bonds of the methoxy groups are also shortened by 0.05 Å, the phenolate groups thus closely approaching a quinone character. These structural modifications can be explained by considering that the diradical species directly result from the removal of two electrons which occupy molecular orbitals (MO) featuring π-antibonding character on both C−O bonds. As a consequence, specific rearrangements within the diradical systems are observed featuring longer Zn−O bonds and a metal that is pushed toward the trans quinoline or pyridine nitrogen atoms, resulting in a shortening of the $Zn-N_{quinoline/pyridine}$ bonds.

Electronic Structures of the Diradicals. In this section, we will only discuss the electronic structure of the complexes in the high spin (HS) $S = 1$ state. The spin-density plots of the diradical complexes $(\mathbf{1}^{\bullet\bullet})^{2+}$−$(\mathbf{5}^{\bullet\bullet})^{2+}$ are shown in Figure 8. In $(\mathbf{1}^{\bullet\bullet})^{2+}$−$(\mathbf{5}^{\bullet\bullet})^{2+}$, two full ligand radicals are observed in the spin-density maps which feature typical patterns for phenoxyl radicals, each group carrying one unpaired electron.[25,26] These results are in line with the structural features of the complexes and confirm the direct participation of the ligands to the oxidation processes, as stressed by electrochemical measurements. When looking at the Mulliken spin populations of $(\mathbf{1}^{\bullet\bullet})^{2+}$, $(\mathbf{2}^{\bullet\bullet})^{2+}$, and $(\mathbf{5}^{\bullet\bullet})^{2+}$ in detail, we observe that the diradical complexes display very similar spin distributions that exclusively involve the phenoxyl rings. $(\mathbf{1}^{\bullet\bullet})^{2+}$ presents a positive spin population at O (0.24), C_{ortho} (0.22, 0.11), C_{para} (0.25), and $O_{methoxy}$ (0.13), accounting for 95% of the total spin density. $(\mathbf{2}^{\bullet\bullet})^{2+}$ and $(\mathbf{5}^{\bullet\bullet})^{2+}$ also present a positive spin population at O (0.26), C_{ortho} (0.24, 0.16), and C_{para} (0.32), accounting for 98% of the total spin density. The spin distribution patterns differ slightly for $(\mathbf{3}^{\bullet\bullet})^{2+}$ and $(\mathbf{4}^{\bullet\bullet})^{2+}$, due to the presence of quinoline groups. For $(\mathbf{3}^{\bullet\bullet})^{2+}$, positive spin populations are found on the phenoxyl rings, but they account for only 87% of the total spin density, 13% involving the quinoline groups. A similar situation is observed for $(\mathbf{4}^{\bullet\bullet})^{2+}$, for which phenoxyl rings and quinoline groups share 89% and 11%, respectively, of the total spin density. In the next sections, we will discuss the implications of such spin distribution that might directly affect the magnetic and spectroscopic properties of the diradical complexes. The localized singly occupied molecular orbitals (SOMOs) for the diradical complexes $(\mathbf{1}^{\bullet\bullet})^{2+}$−$(\mathbf{5}^{\bullet\bullet})^{2+}$ are shown in Figure 9. Not surprisingly, all pairs of SOMOs are π-orbitals that are distributed mainly on the two phenoxyl ligands. In the case of $(\mathbf{1}^{\bullet\bullet})^{2+}$, $(\mathbf{2}^{\bullet\bullet})^{2+}$, and $(\mathbf{5}^{\bullet\bullet})^{2+}$ the pairs of SOMOs are exclusively distributed on the phenoxyl ligands. Interestingly, when focusing on $(\mathbf{3}^{\bullet\bullet})^{2+}$ and

(20) Rotthaus, O.; Jarjayes, O.; Thomas, F.; Philouze, C.; Saint-Aman, E.; Pierre, J.-L. *Dalton Trans.* **2007**, 889.
(21) Chaudhuri, P.; Hess, M.; Müller, J.; Hildenbrand, K.; Bill, E.; Weyhermüller, T.; Wieghardt, K. *J. Am. Chem. Soc.* **1999**, *121*, 9599.
(22) Chaudhuri, P.; Hess, M.; Hildenbrand, K.; Bill, E.; Weyhermüller, T.; Wieghardt, K. *Inorg. Chem.* **1999**, *38*, 2781.
(23) Neese, F. *J. Biol. Inorg. Chem.* **2006**, *11*, 702.
(24) Neese, F. *Coord. Chem. Rev.* **2009**, *253*, 526.
(25) Lu, C. C.; Weyhermüller, T.; Bothe, E.; Wieghardt, K. *J. Am. Chem. Soc.* **2008**, *130*, 3181.
(26) Spikes, G. H.; Milsmann, C.; Bill, E.; Weyhermüller, T.; Wieghardt, K. *Inorg. Chem.* **2008**, *47*, 11745.

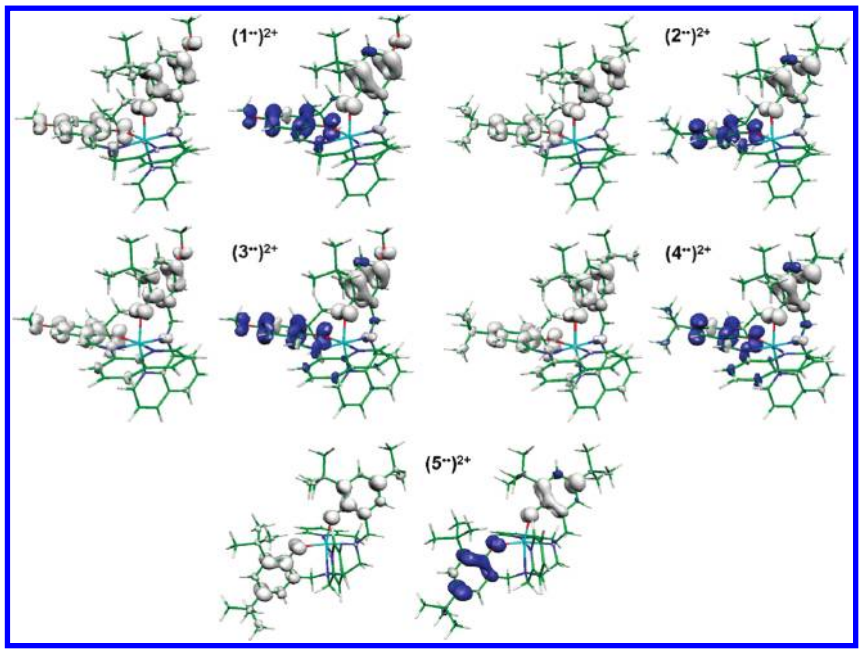

Figure 8. Spin-density plots for (nearly) isoenergetic $S = 1$ (left) and $S = 0$ (right) states of diradical complexes $(\mathbf{1^{\bullet\bullet}})^{2+}$–$(\mathbf{5^{\bullet\bullet}})^{2+}$ (from a Mulliken spin population analysis): (gray) α spin; (blue) β spin. Color scheme for atoms: (light blue) zinc atoms; (dark blue) nitrogen atoms; (red) oxygen atoms; (green) carbon atoms; (white) hydrogen atoms.

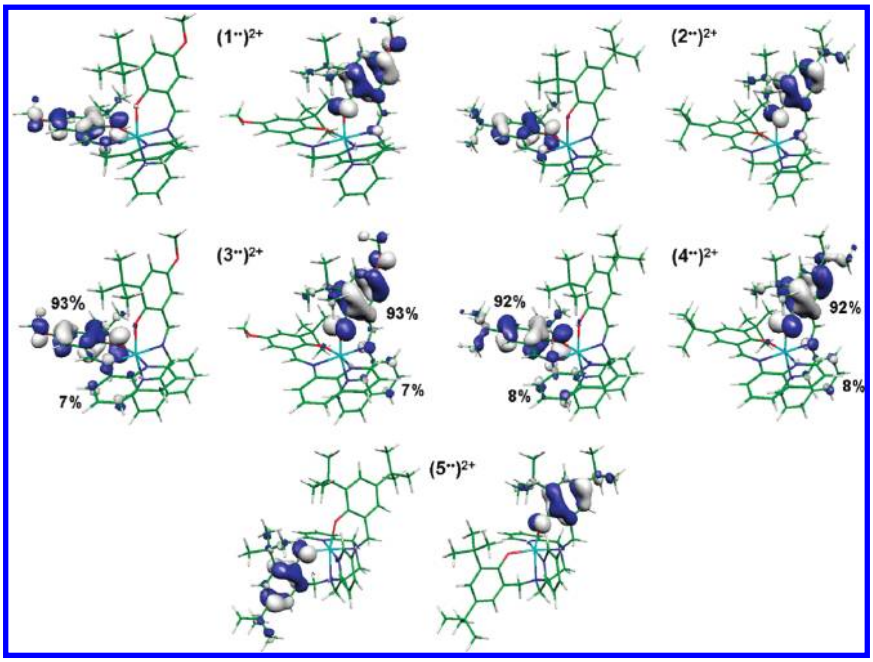

Figure 9. Localized SOMOs of diradical complexes $(\mathbf{1^{\bullet\bullet}})^{2+}$ –$(\mathbf{5^{\bullet\bullet}})^{2+}$. The populations of the SOMOs are indicated in percentages.

$(\mathbf{4^{\bullet\bullet}})^{2+}$, we observe that the SOMOs present significant contributions (7% and 8%, respectively) from the neighboring quinoline groups, likely resulting from their conjugation with the phenoxyl rings.

Exchange Coupling Constants. Since all diradical complexes $(\mathbf{1^{\bullet\bullet}})^{2+}$–$(\mathbf{5^{\bullet\bullet}})^{2+}$ feature two unpaired electrons carried by the ligands, they constitute a set of magnetically coupled systems[27,28] that consist of two spin sites interacting through the Heisenberg exchange couplings J. They can be described by the isotropic Heisenberg–Dirac–van Vleck Hamiltonian:[29–32]

$$H_{\text{eff}} = -2\sum_{i<j} J_{ij}\hat{S}_i \cdot \hat{S}_j \qquad (2)$$

where $\hat{S}_i$ is the spin operator of the ith magnetic center. For the modeling of the magnetic properties of the

(27) Bencini, A.; Gatteschi, D. *EPR of Exchange Coupled Systems*; Springer-Verlag: Berlin, 1990.
(28) Kahn, O. *Molecular Magnetism*; VCH: New York, 1993.
(29) Heisenberg, W. *Z. Phys.* **1926**, *38*, 411.
(30) Heisenberg, W. *Z. Phys.* **1928**, *49*, 619.
(31) Dirac, P. A. M. *Proc. R. Soc. London, Ser. A* **1929**, *A123*, 714.
(32) Van Vleck, J. H. *The Theory of Electronic and Magnetic Susceptibilies*; Oxford University Press: London, 1932.

Table 7. Calculated Exchange Coupling Constants (J) and Spatial Overlaps (S) between the Ligand SOMOs for Diradical Complexes of **1**−**5**

complex	J (cm^{-1})	S
$(\mathbf{1}^{\bullet\bullet})^{2+}$	−10.92	0.060
$(\mathbf{2}^{\bullet\bullet})^{2+}$	−7.27	0.053
$(\mathbf{3}^{\bullet\bullet})^{2+}$	−3.59	0.047
$(\mathbf{4}^{\bullet\bullet})^{2+}$	−1.88	0.045
$(\mathbf{5}^{\bullet\bullet})^{2+}$	+1.49	0.009

present diradical systems, the broken symmetry (BS) approach was used. This approach allows the spin-up and spin-down electrons to be localized on different areas of the molecule so that they can be coupled magnetically but are not forcibly paired.[33−35]

Exchange couplings J are calculated by using the Yamaguchi formula, which covers consistently the whole range of situations from the strong to the weak exchange coupling limit:[36,37]

$$J = -\frac{E_{HS} - E_{BS}}{\langle \hat{S}^2 \rangle_{HS} - \langle \hat{S}^2 \rangle_{BS}} \quad (3)$$

The computed values of the exchange couplings J for diradical complexes $(\mathbf{1}^{\bullet\bullet})^{2+}$−$(\mathbf{5}^{\bullet\bullet})^{2+}$ are listed in Table 7, along with the spatial overlaps S between the two magnetic pairs of ligand−ligand spin vectors. The spin-density plots of the BS states are depicted in Figure 8. They confirm the presence of phenoxyl radicals for $(\mathbf{1}^{\bullet\bullet})^{2+}$−$(\mathbf{5}^{\bullet\bullet})^{2+}$ featuring one unpaired electron per ligand. Focusing on the magnitude of calculated exchange parameters, we observe that all complexes feature weak exchange interaction, with J values varying within an absolute range of 12 cm^{-1}. When comparing $(\mathbf{1}^{\bullet\bullet})^{2+}$ and $(\mathbf{2}^{\bullet\bullet})^{2+}$ to $(\mathbf{3}^{\bullet\bullet})^{2+}$ and $(\mathbf{4}^{\bullet\bullet})^{2+}$, we notice a decrease of the calculated J values for the complexes featuring quinoline rings, which might be related to the extra delocalization of the spin density onto these groups. The most interesting result lies in the computed J value for $(\mathbf{5}^{\bullet\bullet})^{2+}$, which is positive (+1.49 cm^{-1}), whereas negative J values were obtained for $(\mathbf{1}^{\bullet\bullet})^{2+}$−$(\mathbf{4}^{\bullet\bullet})^{2+}$ (−10.92, −7.27, −3.59, and −1.88 cm^{-1}, respectively). In other terms, the two radicals are ferromagnetically coupled ($S = 1$) in $(\mathbf{5}^{\bullet\bullet})^{2+}$, whereas they are antiferromagnetically coupled ($S = 0$) in $(\mathbf{1}^{\bullet\bullet})^{2+}$−$(\mathbf{4}^{\bullet\bullet})^{2+}$. These results turn out to be in very good agreement with experimental data, which evidenced the particular behavior of $(\mathbf{5}^{\bullet\bullet})^{2+}$ by comparing the temperature dependence of the spin triplet of the five complexes. Moreover, the findings are emphasized when looking at the calculated S values for $(\mathbf{1}^{\bullet\bullet})^{2+}$−$(\mathbf{5}^{\bullet\bullet})^{2+}$. A nearly zero spatial overlap of the ligand SOMOs is obtained for $(\mathbf{5}^{\bullet\bullet})^{2+}$, which shows that the radicals interact very weakly with each other. For $(\mathbf{1}^{\bullet\bullet})^{2+}$−$(\mathbf{4}^{\bullet\bullet})^{2+}$ the calculated spatial overlaps present larger values confirming a (weak) antiferromagnetic interaction between the ligand-based radicals. Finally, one can relate the difference of magnetic interaction within the five complexes to their geometrical features. Indeed, $(\mathbf{1}^{\bullet\bullet})^{2+}$−$(\mathbf{4}^{\bullet\bullet})^{2+}$ are characterized by a nearly orthogonal orientation of the phenoxyl rings featuring an angle comprised between 78 and 86°, whereas in the case of $(\mathbf{5}^{\bullet\bullet})^{2+}$ the angle between the two phenoxyl planes is much larger (159°). Therefore, a parallel or antiparallel alignement of the spins will be favored when the two phenoxyl rings will be planar or orthogonal to each other, respectively. Interestingly, when comparing the structures of $(\mathbf{4}^{\bullet\bullet})^{2+}$ and $(\mathbf{5}^{\bullet\bullet})^{2+}$ with those obtained experimentally for the neutral species, we observed a similar orientation of the phenoxyl rings for **4** and **5** with angles of 69 and 160°, respectively. Consequently, it should be possible to predict the sign of the J value on the basis of structural characterizations of the neutral complexes.

Table 8. Calculated EPR Parameters (D, E/D) for Diradical Complexes of **1**−**5**

complex	D (cm^{-1})	E/D
$(\mathbf{1}^{\bullet\bullet})^{2+}$	−0.0143	0.020
$(\mathbf{2}^{\bullet\bullet})^{2+}$	−0.0154	0.023
$(\mathbf{3}^{\bullet\bullet})^{2+}$	−0.0134	0.023
$(\mathbf{4}^{\bullet\bullet})^{2+}$	−0.0150	0.026
$(\mathbf{5}^{\bullet\bullet})^{2+}$	−0.0107	0.004

Zero Field Splittings. The zero-field splitting (ZFS) is typically the leading term in the spin Hamiltonian (SH) for magnetic systems with a total ground spin state $S > {}^1/_2$.[24,38] It is well-known that the spin−spin (SS) contribution of the ZFS (D^{SS}) is dominant in organic triplets and diradicals.[39] This term is a first-order term which involves direct dipolar spin−spin interaction between pairs of electrons.[40,41] Within a DFT framework, the tensor components of D^{SS} may be calculated from the equation of McWeeny and Mizuno.[42] For a system consisting of two unpaired electrons in the SOMOs i and j, this equation can be expanded in the MO basis as follows:

$$D_{KL}^{(SS)} = -\frac{g_e^2 \quad \alpha}{8\, S(S+1)} \cdot [\langle ii|g^{KL}|jj\rangle - \langle ij|g^{KL}|ij\rangle] \quad (4)$$

where g_e is the free electron g value (2.002 319...), α is the fine structure constant (∼1/137 in atomic units), and $g^{KL} = r_{12}{}^{-5}\,(3r_{12,K}r_{12,L} - \delta_{KL}r_{12}{}^2)$ is the operator for the electron−electron magnetic dipole−dipole interaction. Equation 4 consists of two parts that are the "Coulomb" (long-range) contribution and the "exchange" (short-range) contribution, respectively. The latter term is of fundamentally different origin than the isotropic Heisenberg type exchange interaction[27,28] and represents a quantum-mechanical correction to magnetic dipole−dipole interaction.

The computed EPR parameters for diradical complexes of **1**−**5** are given in Table 8, where D values (SS contribution to the ZFS) as well as the E/D ratios are

(33) Noodleman, L. *J. Chem. Phys.* **1981**, *74*, 5737.
(34) Noodleman, L.; Case, D. A. *Adv. Inorg. Chem.* **1992**, *38*, 423.
(35) Noodleman, L.; Davidson, E. R. *Chem. Phys.* **1986**, *109*, 131.
(36) Soda, T.; Kitagawa, Y.; Onishi, T.; Takano, Y.; Shigeta, Y.; Nagao, H.; Yoshika, Y.; Yamaguchi, K. *Chem. Phys. Lett.* **2000**, 223.
(37) Yamaguchi, K.; Takahara, Y.; Fueno, T. In *Applied Quantum Chemistry, V*; Smith, V. H., Ed.; Reidel: Dordrecht, The Netherlands, 1986.
(38) Neese, F. In *High-Resolution EPR*; Hanson, G., Berliner, L., Eds.; Springer-Verlag: New York, 2009; Biological Magnetic Resonance *28*, Chapter 5 (Spin Hamiltonian Parameters from First Principle Calculations: Theory and Application).
(39) Sinnecker, S.; Neese, F. *J. Chem. Phys. A* **2006**, *110*, 12267.
(40) Harriman, J. E., *Theoretical Foundations of Electron Spin Resonance*; Academic Press: New York, 1978.
(41) McWeeny, R. *Methods of Molecular Quantum Mechanics*; Academic Press: London, 1992.
(42) McWeeny, R.; Mizuno, Y. *Proc. R. Soc. London, Ser. A* **1961**, *A259*, 554.

reported. For the analysis of our results, it is worth noting that we do not use the popular point−dipole approximation which connects the ZFS parameter to the interpsin distance in organic radicals.[43] Indeed, a recent computational study pointed out the failure of this model when dealing with delocalized systems and advocates the direct use of quantum-chemical calculations to rationalize experimental data.[44] On first look at the E/D values for $(\mathbf{1}^{\bullet\bullet})^{2+}$−$(\mathbf{5}^{\bullet\bullet})^{2+}$, good agreement with experiment is obtained, since all systems are found to be axial with calculated ratios that are nearly zero. Focusing now on the D values, the "Coulomb" term is the major contribution to the ZFS, the calculated "exchange" contribution being almost negligible for all complexes, since it represents only 1% of the final D values. Most interestingly, we observe a decrease in the computed D values when comparing $(\mathbf{2}^{\bullet\bullet})^{2+}$ to $(\mathbf{1}^{\bullet\bullet})^{2+}$, as well as $(\mathbf{4}^{\bullet\bullet})^{2+}$ to $(\mathbf{3}^{\bullet\bullet})^{2+}$, which is in agreement with experimental data. The present lowering of the ZFS is directly related to the chemical nature of the substituents of the phenoxyl rings. Indeed, when going from $(\mathbf{2}^{\bullet\bullet})^{2+}$ to $(\mathbf{1}^{\bullet\bullet})^{2+}$ or from $(\mathbf{4}^{\bullet\bullet})^{2+}$ to $(\mathbf{3}^{\bullet\bullet})^{2+}$, the *p-tert*-butyl group is replaced by a *p*-methoxy group, leading to an extra delocalization of the spin density onto the $O_{methoxy}$ and to a decrease of the ZFS for $(\mathbf{1}^{\bullet\bullet})^{2+}$ and $(\mathbf{3}^{\bullet\bullet})^{2+}$. Similar analysis applies when comparing $(\mathbf{1}^{\bullet\bullet})^{2+}$ and $(\mathbf{2}^{\bullet\bullet})^{2+}$ to $(\mathbf{3}^{\bullet\bullet})^{2+}$ and $(\mathbf{4}^{\bullet\bullet})^{2+}$, respectively, the latter systems featuring smaller D values, as stressed by EPR measurements. This lowering is again related to the chemical nature of the ligands: replacement of the pyridine group by a quinoline group results in an extra delocalization of the spin density onto these latter ring, which leads to a decrease of the ZFS for $(\mathbf{3}^{\bullet\bullet})^{2+}$ and $(\mathbf{4}^{\bullet\bullet})^{2+}$. To summarize, variation of the ZFS parameters can be simply rationalized by inspecting the chemical nature of the ligand-based radicals. In addition, a general good agreement between theory and experiment is found when comparing the magnitudes as well as the trends of the ZFS parameters, thus confirming the usefulness of quantum-chemical calculations for such studies.

Optical Properties of the Quinoline Derivative Monoradicals. Monoradical species were experimentally characterized, and specific features were observed for the case of complexes **3** and **4** with regard to their optical properties. Here we briefly report our computational results when investigating the electronic structure of these two monoradicals that were primarily optimized as described in the Experimental Section. The spin-density plots of $(\mathbf{3}^{\bullet})^{+}$ and $(\mathbf{4}^{\bullet})^{+}$ are depicted in Figure S6 (Supporting Information) and show that both systems present a similar spin distribution with a full delocalization of the unpaired electron on the ligands. Such observation was expected, since the resulting structures were found to be highly symmetric due to the chemical equivalence of the ligands. When looking at the spin populations in detail, a partial delocalization of the spin density occurs on the quinoline rings, similar to the results obtained for the diradical species. For $(\mathbf{3}^{\bullet})^{+}$ and $(\mathbf{4}^{\bullet})^{+}$ positive spin populations are found on the quinoline groups, accounting for

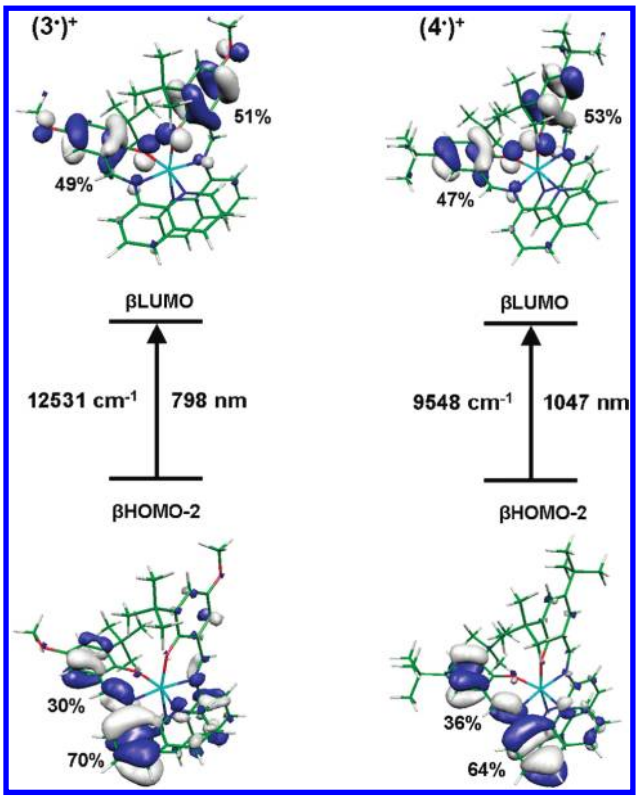

Figure 10. TDDFT assignment of the calculated low-energy transitions for monoradical complexes $(\mathbf{3}^{\bullet})^{+}$ and $(\mathbf{4}^{\bullet})^{+}$. The populations of the relevant MOs (HOMO, highest occupied molecular orbital; LUMO, lowest unoccupied molecular orbital) are indicated in percentages, as well as the energies of the optical transitions.

18% and 14%, respectively, of the total spin density. The localized SOMOs for the two monoradical complexes are depicted in Figure S7 (Supporting Information). These SOMOs are π-orbitals distributed on the two phenolate ligands[45,46] and present significant contributions (8% and 10%, respectively) from the neighboring quinoline groups, as observed for the corresponding diradical species. Preliminary TD-DFT[47,48] calculations were then performed to investigate the optical properties of the monoradical complexes of **3** and **4**. Figure 10 shows the two low-energy transitions that are characteristic for $(\mathbf{3}^{\bullet})^{+}$ and for $(\mathbf{4}^{\bullet})^{+}$ as well as the MOs involved in these transitions. The principal calculated electronic excitations (73% and 70%, respectively) that contribute to these low-energy absorptions ($f = 0.030$ and $f = 0.037$, respectively) are β-HOMO → β-LUMO transitions.[45,46] Both donor orbitals are delocalized π-orbitals that are distributed mainly on one of the ligands with contributions from both phenolate and quinoline groups. Both acceptor orbitals are also delocalized π-orbitals but feature contributions from the phenolate groups of both ligands. Finally, a reasonably good agreement between theory and experiment is found regarding the energies of

(43) Bertrand, P.; More, C.; Guigliarelli, B.; Fournel, A.; Bennett, B.; Howes, B. *J. Am. Chem. Soc.* **1994**, *116*, 3078.
(44) Riplinger, C.; Kao, J. P. Y.; Rosen, G. M.; Kathirvelu, V.; Eaton, G. R.; Eaton, S. S.; Kutateladze, A.; Neese, F. *J. Am. Chem. Soc.* **2009**, *131*, 10092.
(45) Storr, E.; Wasinger, C.; Pratt, R. C.; Stack, T. D. P. *Angew. Chem., Int. Ed.* **2007**, *46*, 5198.
(46) Shimazaki, Y.; Stack, T. D. P.; Storr, T. *Inorg. Chem.* **2009**, *48*, 8383–8392.
(47) Casida, M. E. In *Recent Advances in Density Functional Methods*; Chong, D. P., Ed.; World Scientific: Singapore, 1995.
(48) Stratmann, R. E.; Scuseria, G. E.; Frisch, M. J. *Chem. Phys. Rev.* **1998**, *109*, 8218.

the absorptions: i.e. 12 531 cm^{-1} vs 11 252 cm^{-1} for $(\mathbf{3}^{\bullet})^{+}$ and 9548 cm^{-1} vs 9913 cm^{-1} for $(\mathbf{4}^{\bullet})^{+}$. In addition, the ligand−ligand character that was experimentally assigned to these near-IR transitions is nicely reproduced by our calculations. Our results show that these absorptions are not intraligand charge transfer transitions but rather involve interligand excitations, which is in line with the delocalized character of these monoradicals.

Conclusion

In summary, mono- and bis-Zn coordinated phenoxyl complexes featuring an octahedral metal ion have been prepared. The redox potentials of the Zn−bis-phenolate precursors are found to be ca. 0.1 V higher than for the nickel analogues for which metal-centered or ligand-centered redox processes were evidenced (depending on the ligand). This observation combined with the fact that the oxidation is forced to be ligand-centered in the zinc complex leads us to suggest that the initial electron transfer is ligand-centered in both zinc and nickel complexes. This initial electron transfer is followed by a second one from the metal to the ligand in some nickel complexes.

UV−vis spectroscopy reveals that all the zinc radical species exhibit classical phenoxyl bands at 400−440 nm and that only the quinoline derivatives display a strong additional near-IR band (ε = 1650−6000 M^{-1} cm^{-1}) attributed to a CT transition. Interestingly, $(\mathbf{3}^{\bullet})^{+}$ and $(\mathbf{4}^{\bullet})^{+}$ are also the most stable radical species (half-life higher than 90 min at 298 K) due to the efficient spin delocalization over the quinoline moiety. In the two-electron-oxidized species $(\mathbf{1}^{\bullet\bullet})^{2+}$−$(\mathbf{5}^{\bullet\bullet})^{2+}$ the radical spins are weakly magnetically coupled, with $|J|$ values within the 1−12 cm^{-1} range as determined by EPR and confirmed by DFT calculations. Remarkably, the sign of J changes from negative (*antiferromagnetic* coupling) in the Schiff base complexes $(\mathbf{1}^{\bullet\bullet})^{2+}$−$(\mathbf{4}^{\bullet\bullet})^{2+}$ to positive (*ferromagnetic* coupling) in the Mannich base complex $(\mathbf{5}^{\bullet\bullet})^{2+}$. Geometrical changes (orthogonal to parallel alignment of the phenoxyl rings) likely contribute to the observed inversion of ground spin state. Consequently, it should be feasible to predict the sign of the J only on the basis of structural characterizations of the neutral nonradical precursors. The present weak J values allow the determination of the zero field splitting parameters by EPR spectroscopy. The experimental ZFS parameters in the triplet are found to be axial, with $|D|$ values of 0.0163 cm^{-1} for $(\mathbf{1}^{\bullet\bullet})^{2+}$, 0.0182 cm^{-1} for $(\mathbf{2}^{\bullet\bullet})^{2+}$, 0.0144 cm^{-1} for $(\mathbf{3}^{\bullet\bullet})^{2+}$, 0.0160 cm^{-1} for $(\mathbf{4}^{\bullet\bullet})^{2+}$, and 0.0115 cm^{-1} for $(5^{\bullet\bullet})^{2+}$. A good correlation is found between calculated and experimental $|D|$ values. In the Schiff base series spin delocalization over the methoxy para substituent of the phenoxyl and/or the quinoline moiety induces a significant lowering of $|D|$.

Experimental Section

Materials and Methods. All chemicals were of reagent grade and were used without purification. CH_2Cl_2 was anhydrous (>99.8%) and was stored under an Ar atmosphere. NMR spectra were recorded on a Bruker AM 300 (^{1}H at 300 MHz) spectrometer. Chemical shifts are quoted relative to tetramethylsilane (TMS). Mass spectra were recorded on a Thermofinningen (EI/DCI) or a Nermag R101C (FAB+) apparatus. 298 K UV−vis spectra were recorded on a Perkin-Elmer Lambda spectrophotometer. Low-temperature UV/vis visible spectra were recorded on a Cary Varian 50 spectrophotometer equipped with a low-temperature Hellma immersion probe (1.000 cm path length) and a RK8 KS Lauda cryostat. X-Band EPR measurements have been performed using either a Bruker ESP 300E spectrometer equipped with a Bruker nitrogen flow cryostat or a Bruker EMX Plus spectrometer, equipped with an Oxford Helium flow cryostat. They have been simulated using the Bruker SIMFONIA software. Electrochemical measurements were carried out using a CHI 110 potentiostat. Experiments were performed in a standard three-electrode cell under an argon atmosphere. An $Ag/AgNO_3$ (0.01 M) reference electrode was used. All the potentials given in the text are referenced to the regular Fc/Fc^{+} redox couple used as an internal reference. A glassy-carbon-disk electrode (5 mm diameter), which was polished with 1 mm diamond paste, was used as the working electrode. The electrochemical behavior of the ligands and complexes was studied by cyclic voltammetry (CV) and with a rotating-disk electrode (RDE) in CH_2Cl_2 solutions containing 0.1 M tetrabutylammonium perchlorate (TBAP) as supporting electrolyte. Electrolysis was performed at 233 K using a PAR Model 273 potentiostat and a carbon-felt working electrode.

Crystal Structure Analysis. The collected reflections were corrected for Lorentzian and polarization effects but not for absorption. The structures were solved by direct methods and refined with TEXSAN software. All non-hydrogen atoms were refined with anisotropic thermal parameters. Hydrogen atoms were generated in idealized positions, riding on the carrier atoms, with isotropic thermal parameters. CCDC 702093 and CCDC 728453 contain the supplementary crystallographic data for this paper; these data can be obtained free of charge via http://www.ccdc.cam.ac.uk/conts/retrieving.html.

DFT Calculations. All theoretical calculations were based on density functional theory (DFT) and have been performed with the ORCA program package.[49] Since X-ray structures are not available for all systems under investigation, full geometry optimizations were carried out for the whole set of complexes in their neutral and radical forms. For that purpose, the GGA functional BP86[50−52] was employed in combination with the TZVP[53] basis set for all atoms by taking advantage of the RI approximation with the auxiliary TZV/J Coulomb fitting basis sets.[54] Increased integration grids (Grid4 in ORCA convention) and tight SCF convergence criteria were used. The Heisenberg isotropic exchange coupling constants J were obtained from additional single-point calculations. For that purpose, BS-DFT calculations were performed using the hybrid functional B3LYP[55,56] and the TZVP basis set. The Yamaguchi formula[36,37] was used to estimate the exchange coupling constants J. The zero-field splitting parameters were also obtained from additional single-point calculations employing the B3LYP density functional and the EPR-II[57] basis set. The spin−spin contribution to the ZFS was calculated on the basis of the UNO[39] determinant. Optical properties were investigated employing TD-DFT[47,48] calculations at the B3LYP level in combination with the TZVP basis set. The MO pictures were generated using natural orbitals which were localized according to the Pipek−Mezey criterion[58] as implemented in ORCA.

(49) Neese, F. *ORCA-an ab initio, Density Functional and Semiempirical Program Package* (*v. 2.6-35*); Universität Bonn, Bonn, Germany, **2007**.
(50) Perdew, J. P. *Phys. Rev. B* **1986**, *33*, 8822.
(51) Perdew, J. P. *Phys. Rev. B* **1986**, *34*, 7406.
(52) Becke, A. D. *Phys. Rev. A* **1988**, *38*, 3098.
(53) Schäfer, A.; Huber, C.; Ahlrichs, R. *J. Chem. Phys.* **1994**, *100*, 5829.
(54) Weigend, A. *Phys. Chem. Chem. Phys.* **2006**, *8*, 1057.
(55) Becke, A. D. *J. Chem. Phys.* **1993**, *98*, 5648.
(56) Lee, C.; Yang, W.; Parr, R. G. *Phys Rev. B* **1988**, *37*, 785.
(57) Barone, V., *Recent Advances in Density Functional Methods, Part I.*, Chong, D. P. Ed. World Scientific: Singapore, 1996.
(58) Pipek, J.; Mezey, P. G. *J. Chem. Phys.* **1989**, 4916.

Preparation of the Ligands and Complexes. The ligands $HL^1-H_2L^5$ have been synthesized according to published procedures.[6−8]

Complex 1. To a strirred solution of HL^1 (50.9 mg, 0.171 mmol) in methanol (6 mL) were added a methanolic concentrated solution of $Zn(OAc)_2\cdot 2H_2O$ (18.7 mg, 0.085 mmol) and 1 equiv of triethylamine (24 μL, 0.171 mmol). A yellow precipitate of **1** formed, which was collected by filtration after 3 h of stirring, washed with a methanol/diethyl ether (1/1) mixture, and recrystallized by slow evaporation of methanol. Yield: 24 mg (42%). Anal. Calcd for **1**, $C_{36}H_{42}N_4O_4Zn$: C, 65.50; H, 6.41; N, 8.49. Found: C, 65.70; H; 6.62; N, 8.23. ESI MS: m/z 659.3 for $[\mathbf{1}+H]^+$.

Complex 2. To a stirred solution of HL^2 (34.1 mg, 0.105 mmol) in methanol/CH_2Cl_2 (1/1) (6 mL) were added 1 equiv of triethylamine (15 μL, 0.105 mmol) and a concentrated methanolic solution of $Zn(OAc)_2\cdot 2H_2O$ (11.6 mg, 0.053 mmol). After 12 h of stirring the solution was evaporated, and the resulting solid was dissolved in CH_2Cl_2 and extracted with water. The organic phases were combined, dried over Na_2SO_4, and evaporated, affording a yellow powder of **2**. Yield: 20 mg (53%). Anal. Calcd for $C_{42}H_{54}N_4O_2Zn$: C, 70.82; H, 7.64; N, 7.87. Found: C, 70.92; H, 7.44; N, 7.85. ESI MS: m/z 710.3 for $[\mathbf{2}]^+$, 711.3 for $[\mathbf{2}+H]^+$.

Complex 3. To a stirred solution of HL^3 (100 mg, 0.30 mmol) in methanol (15 mL) were added a concentrated methanolic solution of $Zn(OAc)_2\cdot 2H_2O$ (32.9 mg, 0.15 mmol) and 1 equiv of triethylamine (42 μL, 0.30 mmol). A red precipitate of **3** formed, which was collected by filtration after 2 h of stirring and washed with cold methanol. Yield: 75 mg (68%). ^{1}H NMR ($CDCl_3$): δ 8.9 (s, 2 H), 8.2 (d, ^3J = 4.35 Hz, 2 H), 8.0 (d, ^3J = 8.21 Hz, 2 H), 7.8 (d, ^3J = 7.05 Hz, 2 H), 7.6 (m, 4 H), 7.1 (m, 2 H), 6.8 (d, ^4J = 3.18 Hz, 2H), 6.5 (d, ^4J = 3.21 Hz, 2 H), 3.7 (s, 6 H), 0.9 (s, 18 H). Anal. Calcd for $C_{42}H_{42}N_4O_4Zn$: C, 68.90; H, 5.78; N, 7.65. Found: C, 69.12; H, 5.59; N, 7.59. MS: m/z 790.2 $[\mathbf{3}+H]^+$.

Complex 4. To a stirred solution of HL^4 (100 mg, 0.28 mmol) in methanol (30 mL) were added a concentrated methanolic solution of $Zn(OAc)_2\cdot 2H_2O$ (30.7 mg, 0.14 mmol) and 1 equiv of triethylamine (39 μL, 0.28 mmol). A dark red precipitate of **4** formed, which was collected by filtration after 3 h of stirring and washed with cold methanol. Recrystallization by slow evaporation of an acetone solution afforded single red crystals of **4**. Yield: 65 mg (57%). ^{1}H NMR ($CDCl_3$): δ 9.0 (s, 2 H), 8.3 (d, ^3J = 4.23 Hz, 2 H), 8.0 (d, ^3J = 8.21 Hz, 2 H), 8.1 (d, ^3J = 8.31 Hz, 2 H), 7.62 (m, 4 H), 7.15 (m, 4 H), 7.0 (d, ^4J = 2.55 Hz, 2 H), 1.3 (s, 6 H), 0.9 (s, 18 H). Anal. Calcd for $C_{48}H_{54}N_4O_2Zn$: C, 73.50; H, 6.94; N, 7.14. Found: C, 73.41; H, 6.59; N, 7.32. MS: m/z 784.3 $[\mathbf{4}+H]^+$.

Complex 5. A methanolic concentrated solution of $Zn(OAc)_2\cdot 2H_2O$ (13.0 mg, 0.059 mmol) was added to a strirred solution of H_2L^5 (40 mg, 0.059 mmol) in methanol/CH_2Cl_2 (1/1) (6 mL) in the presence of 500 μL (excess) of triethylamine. After 3 h the stirring was stopped, and after 1 week of standing at room temperature, a white-colorless powder was obtained and collected by filtration. Recrystallization by slow evaporation of CH_3CN afforded single colorless crystals of **5**. Yield: 22 mg (50%). ^{1}H NMR ($CDCl_3$): δ 8.1 (d, ^3J = 3.35 Hz, 2 H), 7.5 (dd, ^3J = 5.89 Hz, 2 H), 7.03 (dd, ^3J = 6.02 Hz, 2 H), 6.98 (d, ^4J = 2.69 Hz, 2H), 6.75 (d, ^4J = 2.56 Hz, 2H), 6.70 (d, ^3J = 7.68 Hz, 2 H), 4.1 (2 × d, ^2J = 10.75 Hz, ^2J = 15.75 Hz, 4 H), 3.6 (d, ^2J = 16.64 Hz, 2 H), 3.3 (d, ^2J = 10.75 Hz, 2 H), 1.3 (s, 18 H), 1.2 (s, 18 H). Anal. Calcd for $C_{44}H_{60}N_4O_2Zn$: C, 71.19; H, 8.15; N, 7.55. Found: C, 71.50; H, 8.01; N, 7.41. ESI MS: m/z 641.4 for $[\mathbf{5}+H]^+$.

Supporting Information Available: CIF files giving crystallographic data for **4** and **5**. UV/Vis monitoring of the titration of **5** by $HClO_4$; fit of IT as a function of T for $(\mathbf{1}^{\bullet})^+$, $(\mathbf{2}^{\bullet})^+$,$(\mathbf{3}^{\bullet})+$, $(\mathbf{4}^{\bullet})^+$; spin-density plots and localized SOMO of $(\mathbf{3}^{\bullet})^+$ and $(\mathbf{4}^{\bullet})^+$. This material is available free of charge via the Internet at http://pubs.acs.org.